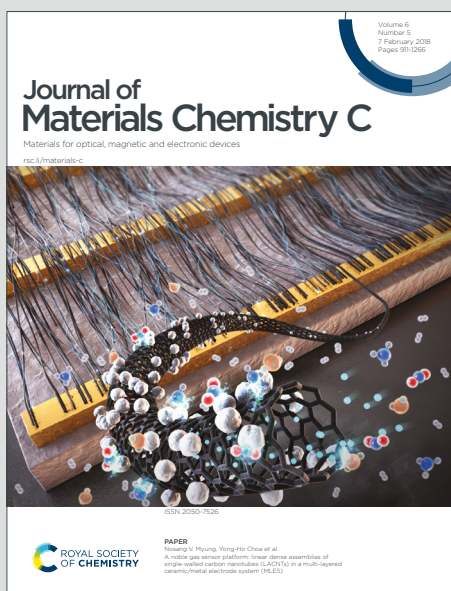


Journal of Materials Chemistry C

Materials for optical, magnetic and electronic devices

Accepted Manuscript

This article can be cited before page numbers have been issued, to do this please use: S. Zhou, H. Tian, X. Kuang, S. Jin, M. Yu, J. Chen and A. Mao, *J. Mater. Chem. C*, 2023, DOI: 10.1039/D3TC03535B.



This is an Accepted Manuscript, which has been through the Royal Society of Chemistry peer review process and has been accepted for publication.

Accepted Manuscripts are published online shortly after acceptance, before technical editing, formatting and proof reading. Using this free service, authors can make their results available to the community, in citable form, before we publish the edited article. We will replace this Accepted Manuscript with the edited and formatted Advance Article as soon as it is available.

You can find more information about Accepted Manuscripts in the [Information for Authors](#).

Please note that technical editing may introduce minor changes to the text and/or graphics, which may alter content. The journal's standard [Terms & Conditions](#) and the [Ethical guidelines](#) still apply. In no event shall the Royal Society of Chemistry be held responsible for any errors or omissions in this Accepted Manuscript or any consequences arising from the use of any information it contains.

Cite this: DOI: 00.0000/xxxxxxxxxx

Piezochromic Effect and Low-pressure Superconductivity Discovered in Inorganic Halide Perovskite RbPbI₃

Siyuan Zhou,^{ab‡} Hao Tian,^{c‡} Xiaoyu Kuang,^a Siyu Jin,^a Miao Yu,^a Jichao Chen,^a and Aijie Mao^{*ab}Received Date
Accepted Date

DOI: 00.0000/xxxxxxxxxx

The structural phase evolution and superconductivity of perovskite RbPbI₃ via pressure have been investigated by employing the first-principles calculations. The findings suggest that RbPbI₃ undergoes three structural phase transitions from ppPv-*Pnma* to ppPv-*Pnma*(I) phases at 4.6 GPa, from ppPv-*Pnma*(I) to ppPv-*Pnma*(V) phases at 19 GPa, and from ppPv-*Pnma*(V) to *Pm* phases at 69.2 GPa, respectively. Two novel phases ppPv-*Pnma*(V) and *Pm* are predicted different from other previous reported results. Meanwhile, an obvious piezochromic effect appears in ppPv-*Pnma*(I) phase due to the change of the band gap under pressure tuning. Quite surprisingly, the electron-phonon coupling calculations reveal that ppPv-*Pnma*(V) phase may be a potential low-pressure superconductor with a T_c of 8 K (7.3 K) at 20 GPa, which slight higher than other similar perovskite or alloys (~3K). Our studies further provide a theoretical support for exploring high- T_c low-pressure superconductivity and piezochromic effect in halide perovskites.

1 Introduction

Inorganic lead halide perovskites with the chemical formula APbX₃ (A=alkali cation, X=halide anion) have aroused extensively interest due to its adjustable band gap, long carrier diffusion length, high carrier mobility and other excellent photo-physical properties.^{1–3} Especially for CsPbI₃ and RbPbI₃, are regard as a potential candidate material to improve the stability replacing the organic lead halide perovskite.^{4–6} Thus, numerous experimental and theoretical methodologies focus on the structural stabilities and its applications.^{7,8} Even if CsPbI₃ possesses a suitable bandgap energy 1.73eV for applying in solar cells, the structural instability (different phases *Pnma*, *Pm3m*, *P4/mbm* will appear at different temperature) further limits its practical application. Whereas, for RbPbI₃, an orthorhombic *Pnma* phase persists at temperature range from 200 K to 400 K, no other phase is observed.⁹ Meanwhile, by adding the RbI to Formamidinium-based perovskites can suppress its "yellow-phase impurity", and turn forms RbPbI₃ impurities, which achieved in excellent power output.¹⁰ Moreover, δ -RbPbI₃ has suitable band alignment with

TiO₂ effectively carried out the electron transfer, which can be regarded as a potential solar cell material.¹¹ Of course, low dimensional RbPbI₃ nanowire also presents a good photoresponsive activity when the absorption wavelength is below 450nm.^{12,13} All of the aforementioned merits indicate that RbPbI₃ is worth paying attention to, even if it does not have a suitable band gap as CsPbI₃ does. Nevertheless, crystal structure and structural phase transition are the most fundamental issue in understanding and improving their performance. To the best of our knowledge, most experiments and theories focus on investigating the structure characteristic of CsPbI₃ via dopants, dimensional reduction, and pressure,^{14,15} and less involves RbPbI₃, especial in high-pressure.

Pressure is regarded as an effective avenue to tune the crystal structures and physical properties of perovskite materials.¹⁶ By applying a hydrostatic pressure, all kinds of structural phases (such as *Pmn2₁*, *Pm*, *P2₁/c*, *P2₁/m*, post-perovskite (pPv), post-post-perovskite (ppPv), *I4mm*, and so on) emerge.^{5,6,16,17} More importantly, pPv structure appeared in MgSiO₃ explains satisfactorily the existence of anisotropic features in the D' layer of Earth, which was discovered in some ABX₃ compounds and was transformed from Pv (perovskite structure) under pressure.¹⁸ Recent progress on pressure-induced structure further reveals that a novel stable post-post-perovskite (ppPv) structure has been obtained in numbers of ABO₃, ABF₃, and A₂O₃ materials under pressure, explaining successfully the "N phase" as discovered in experiment.^{19–21} This ppPv structure is composed of a three-dimensional network of edge-sharing oxygen or fluorine octahe-

^a Institute of Atomic and Molecular Physics, Sichuan University, Chengdu 610065, China

^b College of Physics, Sichuan University, Chengdu 610064, China; E-mail: scu_mij@126.com

^c School of Physics and Electronic Engineering, Zhengzhou Normal University, Zhengzhou 450044, China

† Electronic Supplementary Information (ESI) available. See DOI: 00.0000/00000000.

‡ S.-Y. Z. and H. T. contributed equally to this work.

dra, unlike traditional ABX_3 perovskite structure (Pv) which is composed of corner-sharing $[BX_6]^{4-}$ octahedra, even though they both belong to the same point group $Pnma$.¹⁹ As the research progressed, ppPv structures present heterogeneous, which can be divided to ppPv- $Pnma$ (I), ppPv- $Pnma$ (II), and ppPv- $Pnma$ (III) according to the connection mode of among octahedra or polyhedra.^{19,22} Meanwhile, the detailed structural characteristic of $RbPbI_3$ in experiment is along b direction of the crystal of double rows of edge-sharing PbI_6 octahedra, which is consistent with that of the aforementioned ppPv structure.¹⁹ Taken the diversity of ppPv structure into account, it is unknown whether the new ppPv structure or other novel structures will emerge under high pressure for $RbPbI_3$.

Usually, whether perovskite oxide or perovskite halide, appears as insulator at ambient temperature and pressure. It is remarkably, however, the insulator can become a metal by applying pressure in perovskite oxide $CaZrO_3$.²² This offers the possibility for further exploring superconductivity in perovskite materials. Up to now, research on the superconductivity of hydrides is quite hot due to the higher superconducting transition temperature T_c .^{23,24} There are also studies involving the superconductivity of anti-perovskite $CuNNi_3$ and Ca_3PN , and the corresponding superconducting transition temperatures 3.2 K and 4 K are predicted.^{25,26} Of course, the superconductivity are found in other compounds, such as $(Ca_{1-x}Sr_x)Pd_3P$ ($0.17 \leq x \leq 0.55$), $PbVSe_2$ and $Ba_{0.5}Sr_{0.5}Pb_3$.²⁷⁻²⁹ Regrettably, the superconductivity of perovskite halide has not been reported, and even superconductivity of perovskite oxide is rarely reported. Thus, the goal of this work is to predict the novel structural phase of $RbPbI_3$ via pressure, further analyzing the pressure-induced piezochromic effect and superconductivity.

2 Computational details

The pressure-induced piezochromic effect and superconductivity of $RbPbI_3$ have been investigated by means of the Vienna ab initio simulation package (VASP) based on density function theory (DFT) combined with the the Crystal structure Analysis by Particle Swarm Optimization (CALYPSO).³⁰⁻³³ Many of structures of the analogue unit $RbPbI_3$ in 2-4 formula units (f.u.) was searched based on CALYPSO method.^{32,33} The initial structures are randomly generated and subsequently optimized. Each generation comprises 30 structures, with 70% generated through particle swarm optimization and the remaining 30% newly generated in a random fashion. The search process encompasses fifty generations. In the all calculation, PBEsol, PBEsol+SOC, and HSE06 functionals based on the generalized gradient approximation (GGA) are adopted, where, HSE06 functional is mainly used for accurate calculation of band gap.³⁴ The valence electrons of the atoms considered are: Rb $4s^2 4p^6 5s^1$, Pb $5d^{10} 6s^2 6p^2$, I $5s^2 5p^5$. The k-point grid is sampled along the k-tight Monkhorst-packet grid,³⁵ with the minimum allowable spacing between k-points set to 0.1 \AA^{-1} . The k-Monkhorst-packet grid refers to the specified minimum grid density, which is the maximum distance between any two k-points in the grid. Furthermore, a conversion theory was utilized to relate the physical wave function to the auxiliary wave function (projected amplified wave (PAW) method),³⁶

setting the cutoff energy of the wave function to 700 eV. Correspondingly, the convergence thresholds of the energy and Herman Feynman force on any ion were established as 10^{-8} eV and $-10^{-3} \text{ eV \AA}^{-1}$ respectively, where Herman Feynman force refers to the derivative of generalized free energy. Moreover, to ensure structural stability, we use the finite-displacement method for phonon dispersion curve calculations. This involves computing forces in Density Functional Theory (DFT) and determining their derivatives using the finite difference method, illustrated in Figure S1. The calculated different crystal structures were visualized by VESTA software package³⁷ and the space group was determined by FINDSYM program.³⁸ Finally, the electron-phonon coupling is calculated by means of the Quantum-ESPRESSO package based on linear response theory.^{39,40} Utilizing the Standard Solid-State Pseudopotentials (SSSP), we employed pseudopotentials tailored for Rb, Pb and I atoms. Pseudopotential approximation involves substituting the Coulomb potential in the many-electron system Hamiltonian with a smooth function. The calculation employed a k-point grid of $12 \times 16 \times 4$ for each q-point, with a corresponding q-point grid of $3 \times 4 \times 1$. The superconducting transition temperature was simulated by the Allen-Dynes modified McMillan equation.⁴¹ The cutoff energy was set at 100 Ry, and the coulomb pseudopotential was selected as $\mu = 0.1$ and 0.13, respectively.

3 Results and discussion

3.1 Pressure-induced structural phase transitions

Based on the first principles calculations and CALYPSO method, many structures of $RbPbI_3$ are taken into account under pressure of 0-100 GPa. The relations between enthalpies ($\Delta H = E + PV$) and pressures are plotted in Figure 1 for $RbPbI_3$ with different stable phases. Meanwhile, Figure 1 also presents the relation between the volume and pressure for different stable phases.

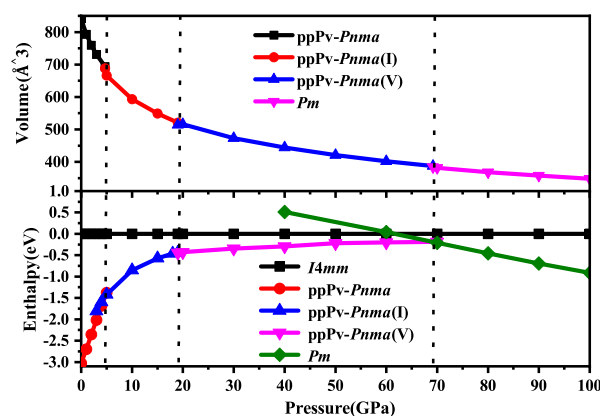


Fig. 1 Volume and enthalpy values were calculated at hydrostatic pressure from 0 to 100 GPa.

From Figure 1, one can see that, $RbPbI_3$ undergoes three structural phase transitions from ppPv- $Pnma$ to ppPv- $Pnma$ (I) phases at 4.6 GPa, from ppPv- $Pnma$ (I) to ppPv- $Pnma$ (V) phases at 19

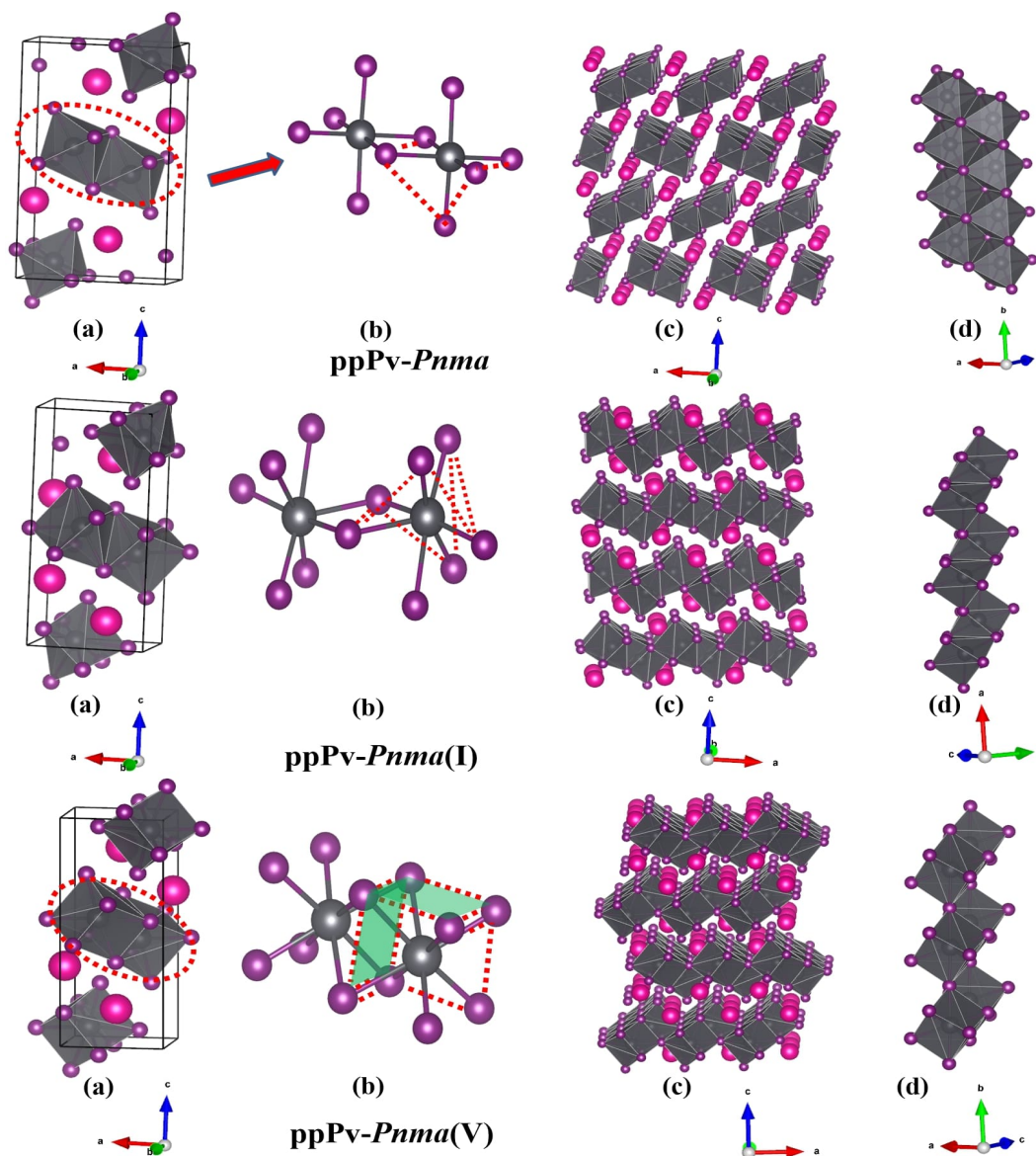


Fig. 2 The schematization of RbPbI_3 is Pv-Pnma , ppPv-Pnma(I) , ppPv-Pnma(V) . The figure to the right of each panel describes the local structure of the adjacent polyhedrons in these structures, and how they are arranged.

GPa, and from ppPv-Pnma(V) to Pm phases at 69.2 GPa, respectively. Here, to distinguish it from the previous studies, the new post-post-perovskite structure is identified as ppPv-Pnma(V) . Of course, the ppPv-Pnma and ppPv-Pnma(I) are employed the same labels in previous reports.²² Regrettably, ppPv-Pnma(II) , ppPv-Pnma(III) and ppPv-Pnma(IV) phases presented in previous studies, as well as $Pnma$, $C2_1/m(\text{I})$ and $C2_1/m(\text{II})$ predicted in CsPbI_3 have not been found in this works.^{17,22,42} In the same time, some structures ($P4/mmm$, $C2mm$, $I4mm$, Cm , and so on) predicted in other halide perovskites may be absent or metastable.^{43,44} Surprisingly, the new crystal phase ppPv-Pnma(V) has never been previously presented in any materials. Moreover, the relation between the volume and pressure in Figure 1 reveals that the phase transitions from ppPv-Pnma to ppPv-Pnma(I) and ppPv-Pnma(V) to Pm belong to a first-order structural phase transitions,

and the phase transition from ppPv-Pnma(I) to ppPv-Pnma(V) belongs to a second-order structural phase transitions. A first-order structural phase transition involves a material undergoing a direct transformation from one crystal structure to another, marked by significant thermodynamic changes such as abrupt jumps in energy, volume, or other physical properties. This results in noticeable discontinuities, distinguishing it from the continuous changes observed in a second-order phase transition.^{45,46}

In order to further understand the characteristics of these stable phases, the schematic view of the corresponding structures are shown in Figure 2, and the corresponding structural parameters are summarized in Table S1 (seen in Support materials). As revealed in Figure 1 and Figure 2(a), the ground state of RbPbI_3 is post-post-perovskite structure (ppPv-Pnma) up to about 4.6 GPa. Table S1 indicates that the structural param-

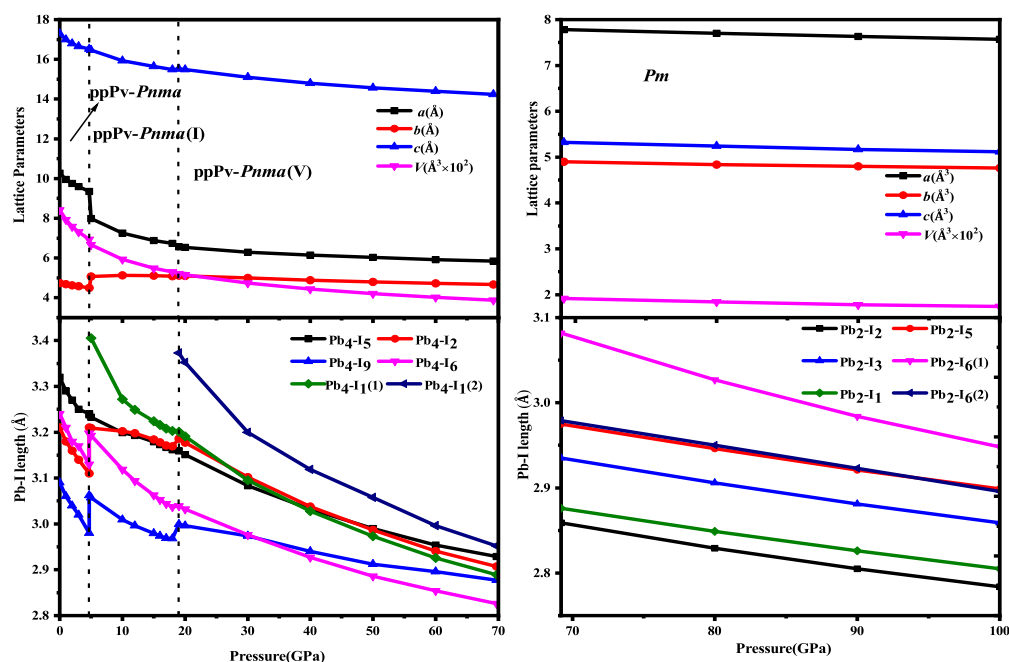


Fig. 3 Lattice parameters and Pb-I length of Pv-*Pnma*, ppPv-*Pnma*(II), ppPv-*Pnma*(V) and *Pm* phases of RbPbI₃ at 0-100 GPa hydrostatic pressure.

eters ($a=10.272 \text{ \AA}$, $b=4.736 \text{ \AA}$, and $c=17.297 \text{ \AA}$) of the ground state for ppPv-*Pnma* phase are in line with the experimental results ($a=10.276 \text{ \AA}$, $b=4.775 \text{ \AA}$, and $c=17.382 \text{ \AA}$).⁹ Meanwhile, Figure 2(a) reveals that ppPv-*Pnma* phase can be characterized by any oxygen octahedron connected to other four oxygen octahedra by four common edges. Note that the coordination around each Pb ion in ppPv-*Pnma* is six I ions due to Pb-I bonds contained two doubly degenerate and other two non-degenerate, and those bonds decrease with increasing pressure seen in Table S1 and Figure S1. On the other hand, the c lattice parameter (17.297 \AA) is significantly elongated, while the b lattice parameter (4.736 \AA) is significantly shortened relative to the a lattice parameter (10.272 \AA), as seen in Table S1. These characteristics of ppPv-*Pnma* phase are similar to those of the ppPv-*Pnma* phase reported by Xu et al., while is different the ppPv-*Pnma*(I) characterized by each oxygen polyhedron connected to other six oxygen polyhedrons by six common edges in previous studies.^{19,22} Moreover, it is clear that the ground state of RbPbI₃ is post-post-perovskite structure (ppPv-*Pnma*) not perovskite structure (*Pnma*) appeared commonly in oxygen perovskites and other halide perovskites.^{19,22,43,44} Of course, in order to further verify the ground state structure, several other possible structures (*Pnma*, ppPv-*Pnma*(*Cmcm*), ppPv-*Pnma*(III), *Pm3m*) appeared in previous reports have also been examined.^{19,22,43,44,47} The calculated results indicate that the energy values (-35.9172 eV) of ppPv-*Pnma* is lower than those of *Pnma* (-35.6253 eV), ppPv-*Pnma*(*Cmcm*) (-35.7586 eV), ppPv-*Pnma*(III) (-34.9954 eV) and *Pm3m* (-34.4393 eV). Meanwhile, the phonon dispersions of ppPv-*Pnma*, *Pnma* and ppPv-*Pnma*(*Cmcm*) shown in Figure S1(a-c) indicate that three structures have no negative phonon frequencies and are dynamically stable. Those further reveals ppPv-*Pnma* is the ground state, which is consistent with the experimental

results,⁹ where *Pnma*, ppPv-*Pnma*(*Cmcm*) phases are possible metastable for RbPbI₃.

As also shown in Figure 1, RbPbI₃ is predicted to undergo a phase transition from a post-post-perovskite structure (ppPv-*Pnma*) to another post-post-perovskite structure about 4.6 GPa. Figure 2(b) clearly presents that any halide polyhedron is connected to six adjacent halide polyhedral by four common edges and two common faces (each face is triangle formed by three common edges) along a axis, which is similar to the characteristics of ppPv-*Pnma*(I) phase in our previous reports.²² For consistency, this post-post-perovskite structure is denoted as ppPv-*Pnma*(I) in the following, and retains the ground state up to about 19 GPa. Moreover, as indicated in Fig S1 (seen in Support materials), the lattice parameters a , b , c and V (volume) of have a sudden change at pressure 4.6 GPa from ppPv-*Pnma* to ppPv-*Pnma*(I) phases, which reveals the phase transition is first-order structural phase transition. Figure S1 and Table S1 also indicate that seven Pb-I bonds of polyhedron in ppPv-*Pnma*(I) phases exist two doubly degenerate and three non-degenerate bonds, and the varietal tendency of Pb-I bond with the pressure is the same to that of ppPv-*Pnma*. Apparently, the coordination of each Pb ion goes from six to seven after phase transition due to add another non-degenerate Pb-I bond in ppPv-*Pnma*(I). Interestingly, for a given pressure 5 GPa (very close to the phase transition pressure 4.6 GPa), one can see that the a ($=7.97 \text{ \AA}$) and b ($=5.07 \text{ \AA}$) lattice constants of ppPv-*Pnma*(I) are 14.4% shorter and 13.7% longer than a ($=9.32 \text{ \AA}$) and b ($=4.46 \text{ \AA}$) lattice constants of ppPv-*Pnma*, as well as the c ($=16.52 \text{ \AA}$) lattice constant of ppPv-*Pnma*(I) have a very small change relative to c ($=16.46 \text{ \AA}$) lattice constant of ppPv-*Pnma*. It means that the phase transition from ppPv-*Pnma* to ppPv-*Pnma*(I) is associated with an alteration in the crystal's structural shape. Even though ppPv-*Pnma* and ppPv-*Pnma*(I)

phases have the same space group (No. 62) and the same types of Wyckoff positions, the changes in lattice constants, the coordination number and the structural shape reveal that it is also a reconstructive phase transition.

When the pressure rises to 19 GPa, another post-post-perovskite structure appears and retains lower enthalpies than ppPv-*Pnma*(I) phases up to 69.2 GPa. Figure 2(c) reveals that this post-post-perovskite structure differs from other post-post-perovskite structures previously reported.²² We also find that the connection mode among the halide polyhedra in this structure is the same as that of ppPv-*Pnma*(III) phase, but there exist some differences (i.e., common faces is almost square formed by four common edges, which different from common face is triangle formed by three common edges in ppPv-*Pnma*(III) phase) in detail. For distinction, this post-post-perovskite structure is marked as ppPv-*Pnma*(V) in this work. As shown in Figure 2(c) and Table S1, Pb-I bonds of polyhedra in ppPv-*Pnma*(V) phases are eight contained two doubly degenerate and four non-degenerate bonds. Interestingly, by analyzing the Figure 1 and Figure S1, the sudden change in the lattice parameters *a*, *b*, *c* and *V* are not observed from ppPv-*Pnma*(I) to ppPv-*Pnma*(V) phases, which reveals the phase transition is second-order structural phase transition. Meanwhile, the transformation from ppPv-*Pnma*(I) to ppPv-*Pnma*(V) results in a change in coordination number from seven to eight only, implying the phase transition is isostructural phase transition similar to the transition from ppPv-*Pnma*(I) to ppPv-*Pnma*(II) in previous reports.²²

To our surprise, other new phase *Pm* is predicted successfully at about 69.2 GPa and retains the most stable up to 100 GPa, which completely differs from the post-post-perovskite structure seen in Figures 2(a-d). As indicated by Figure 2(b,c), any halide polyhedron is connected to other neighboring halide polyhedral via corner sharing along *c* axis and edges sharing on different *c* plane, which is different from the halide octahedra in traditional perovskite via corner sharing each other reported in CsMI₃ (M=Pb and Sn) only.⁴⁸ Moreover, Figure 1, Figure S1 and Table S1, a sudden changes of the lattice parameters *a*, *b*, *c* and *V* (volume) are observed about 69.2 GPa, and the coordination number around Pb retains the same at eight. Meanwhile, *Pm* and ppPv-*Pnma*(V) phase possesses the different space groups and the different types of Wyckoff positions shown in Table S1. The aforementioned discussion further illustrates the transition from ppPv-*Pnma*(V) to *Pm* is both a first-order phase transition and reconstructive phase transition. Of course, by continuing to apply pressure on the ppPv-*Pnma*(V) phase, other phase *P2₁/c* can be obtained at pressure from 69.2 GPa to 100 GPa. In order to further verify the ground state at this pressure region, we employ the CALYPSO search method by fixing the cell of *P2₁/c* or ppPv-*Pnma*(V) phases to obtain other relative stable phases (*Pm*, *Pmn2₁*, *P2₁/c*, *P2₁/m*, *Cmc2*, *Cm*, *Pc* and so on). Their enthalpies and the phonon dispersions further reveal that *Pm* is the most stable at pressure from 69.2 GPa to 100 GPa compared with other phases. Unfortunately, the *Pmn2₁* phase reported in CsPbI₃ is only a metastable phase for RbPbI₃.⁴⁹

3.2 Electric properties and piezochromic effect

Pressure can induce the bond length shortening and the B-X-B angle increasing, which narrows and widens the corresponding band gap, respectively. The "B-X-B angle" refers to the bond angle in a molecule or compound, with X representing one atom and B/B' representing another atom or group. It specifically indicates the angle formed when there is a bond between an atom (X) and two other atoms or groups (B and B') in the molecule. Thus, pressure is regard as a good strategy to regulate the band gap. In this works, based on the stable structures obtained above, the electric band structures are predicted by employing functional PBEsol, HSE06 and PBEsol contained the spin-orbit coupling (SOC) under pressure from 0 to 100 GPa. As depicted in Figure 4, the energy band gap decreases gradually with increasing pressure at the corresponding stable phase pressure region. It can be also seen that the variation tendency of band gap is consistent whether PBEsol or HSE06 functional, which is different from that of PBEsol+SOC. As presented in Figure 4, the tune of pressure on the band gap for ppPv-*Pnma*(I) is very obvious, resulting in appearing the piezochromic effect. That is to say, the band gap of ppPv-*Pnma*(I) decreases from 2 to 0 eV with the pressure varying from 5 to 18 GPa, and undergoes a transition from insulator to metal. Considering the alterations in band gap and pressure, we calculated the piezochromic effect amplitude of ppPv-*Pnma*(I) phase. The amplitude of the piezochromic effect is measured at 0.154 eV/GPa⁻¹, surpassing the 0.058 eV/GPa⁻¹ piezochromic effect observed in the study of BiFeO₃ by Sando et al.,⁵⁰ indicating a significant piezochromic effect of RbPbI₃ under pressure. This piezochromic effect also appeared in ppPv-*Pnma*(II) for CaZrO₃ in previous reports.²² Similarly, this piezochromic effect has also been found in ppPv-*Pnma*(IV) phase of RbSnBr₃ and the non-Pv-*Pnma* phase of CsPbX₃,^{17,42} as well as in the experimental study of Cs₄MnBi₂Cl₁₂ with *Imma* phase and Cs₂CoCl₄ with *Pnma* phase. The above discussion further indicate that the piezochromic effect appears

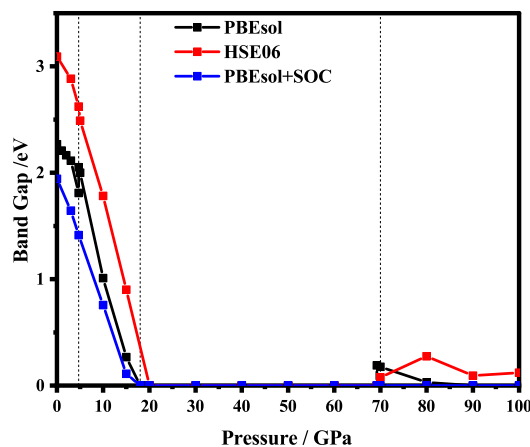


Fig. 4 RbPbI₃ electronic band gap calculated by PBEsol, HSE06 and PBEsol+SOC under hydrostatic pressure of 0-100 GPa.

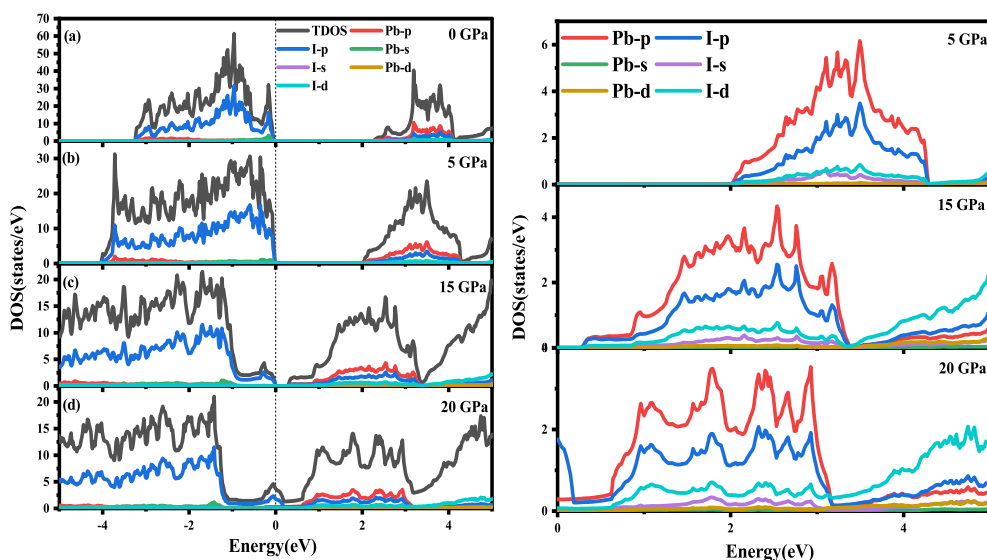


Fig. 5 DOS of RbPbI₃ predicted by PBEsol method under different phase and hydrostatic pressure: (a) ppPv-*Pnma* (0GPa), (b) ppPv-*Pnma*(I) (5GPa), (c) ppPv-*Pnma*(I) (15GPa), (d)ppPv-*Pnma*(V) (20GPa). On the right side is the conduction band corresponding to 5GPa, 15GPa and 20GPa. The dashed line is set to the Fermi level.

in those materials with the same orthorhombic symmetry, which is closely related to the symmetry of structure. Up to now, one can see that the piezochromic effect is very likely to occur when the crystal structure belongs to orthorhombic perovskite-like structure. Of course, it needs to be further verified in theory and experiment.

To explore deeper insight into the effect of pressure on the band gap, the atom-resolved density of states for the corresponding stable phases at certain pressure (0 GPa, 5 GPa, 15 GPa, 20 GPa) are displayed in Figure 5, respectively. As shown in Figure 5(a), at 0 GPa, the conduction band edge is dominated essentially by p orbitals of I and Pb atoms. Whereas, the valence band edge derives primarily from the p orbital of I atom with a very small contribution of s orbital of Pb atom. When pressure is up to 5 or 15 GPa, the contribution of orbit on the conduction and valence band edges is similar to that in 0 GPa. In Surprise, the contribution of I-p state on the conduction band is more and more obvious compared with the p orbital of Pb. As the pressure increases, the p orbitals of I atom shift towards lower energy regions, causing the band gap to decrease. As revealed in Figure 4, RbPbI₃ presents the metallic properties at 18 GPa. When pressure ranges from 0 to 18 GPa, the transition from insulation to semiconductor to metal occurs. Thus, the piezochromic effect appeared in ppPv-*Pnma*(I) is mainly derived from the p orbital of I, which is different from that in CaZrO₃ derived from the d orbital of Zr.

3.3 Superconductivity properties

The aforementioned discussion reveals that RbPbI₃ retains metallic with pressure varying from 20 to 100 GPa, implying that it could be a potential superconductor. Superconductivity relies on a substantial Density of States (DOS) at the Fermi level and high symmetrical crystal structure.^{51,52} DOS, representing

the count of allowable electron states at a specific energy level, aids in understanding the overall distribution of states with respect to energy and unveils energy band spacing in semiconductors. In comparison, more electronic states appear near the Fermi level for RbPbI₃ with ppPv-*Pnma*(V) phase at 20 GPa, revealing ppPv-*Pnma*(V) phase of RbPbI₃ possesses higher superconducting transition temperature. Therefore, we will select ppPv-*Pnma*(V) phase of RbPbI₃ at 20 GPa to explore its superconductivity. Correspondingly, the electron-phonon interaction parameter λ , the Eliashberg phonon spectral function $\alpha^2F(\omega)$ and the logarithmic average of the phonon vibration frequency ω_{log} have been investigated as shown in Figure 6. Based on equation 1, the value 1.16 of the electron-phonon interaction parameter λ is estimated.^{53,54} Where N_{E_F} is the density of electronic states at the Fermi level, $\langle g^2 \rangle$ is the average value of the electroacoustic matrix elements near the Fermi level, M is the atomic mass, and $\langle \omega^2 \rangle$ is the average value of the square of the vibration frequency. Therefore, it can be seen that λ is positively correlated with DOS near Fermi level and negatively correlated with the average value of atomic vibration frequency. Apparently, our calculated parameter λ is higher than some alloys (0.56 for PbVSe₂ at 6.4 GPa, 0.46 for SnVSe₂ and 0.64 for Ti₆Pb₄), and slightly lower than some perovskite (1.43 for MgVH₆ at 150 GPa).^{28,55,56}

$$\lambda = 2 \int_0^{\infty} \frac{\alpha^2 F(\omega)}{\omega} d\omega = \frac{N_{E_F} \langle g^2 \rangle}{M \langle \omega^2 \rangle} \quad (1)$$

$$T_c = \frac{\omega_{log}}{1.2} \exp \left(-\frac{1.04(1 + \lambda)}{\lambda - \mu^*(1 + 0.62\lambda)} \right) \quad (2)$$

$$\omega_{log} = \exp \left[\frac{2}{\lambda} \int_0^{\infty} \frac{d\omega}{\omega} \alpha^2 F(\omega) \ln(\omega) \right] \quad (3)$$

When λ is less than 1.5, the superconducting critical tempera-

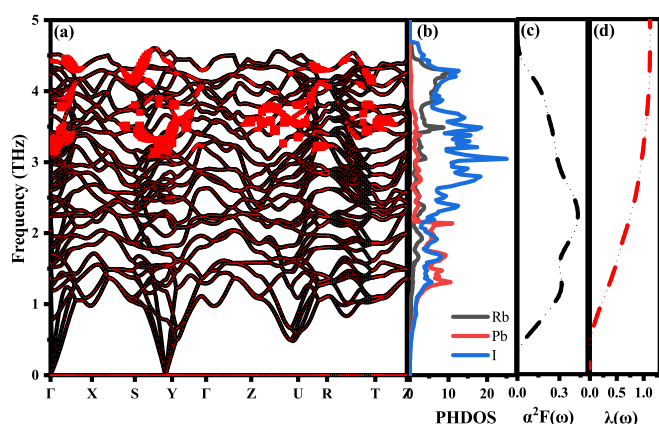


Fig. 6 (a) Phonon spectrum decorated by the normalization phonon linewidth; (b) The projected phonon state density is calculated; (c) Ellyashberg spectral function $\alpha^2F(\omega)$; (d) Cumulative EPC strength λ of the ppPv-*Pnma*(V) phase of RbPbI₃ at 20 GPa.

ture T_c can be calculated by the Allen-Dynes modification of the McMillan formula as seen in equation 2 and 3. Where μ^* represents the shielded anti-superconducting Coulomb pseudopotential. When μ^* is set to 0.1 and 0.13, the corresponding T_c value of ppPv-*Pnma*(V) in RbPbI₃ is about 8 and 7.3 K at 20 GPa, respectively. Meanwhile, we also estimate the T_c of ppPv-*Pnma*(V) with 3.8 K at 60 GPa (see Figure S2), which is smaller than that at 20 GPa. It may be attributed to the smaller DOS value at the Fermi level at 60 GPa.

To effectively explain the electronic coupling mechanism on which superconductivity depends, we give PHDOS, $\alpha^2F(\omega)$ and $\lambda(\omega)$ are drawn in Figure 6. Figure 6 (a) shows the phonon spectrum modified by normalized phonon linewidth. The phonon linewidth is closely associated with the electron-phonon interaction matrix element, describing the scattering probability amplitude of phonons with a wave vector q on the Fermi surface (FS).⁵⁷ Compared with the cutoff frequency of δ -CsPbI₃, the frequency of the largest RbPbI₃ is increased by 24%,⁵⁸ which may be attributed to the high-frequency modes of RbPbI₃ contributed mainly by the vibration of the I and Rb atoms. This enhancement is due to the vibration of Rb atoms, proving beneficial for improving T_c . In contrast to low-frequency acoustic modes, high-frequency optical phonons contributed by Rb and I atoms exhibit stronger electroacoustic coupling, driven by their larger phonon linewidth. As revealed in Figure 6(b), it is not difficult to see that the vibration frequency in the low frequency region (less than 2.5 THz) is mainly contributed by Pb and I atoms, while that in the high frequency region (higher than 2.5 THz) is mainly related to I atoms, and a large number of electrons are transferred from I-p to Pb-p with resulting in the strong hybridization of p-p orbitals. Electron transfer between Pb and I atoms leads to electron scattering in the lattice, which increases electron-phonon coupling. Thus, the superconductivity of RbPbI₃ is mainly contributed by p orbital which is different from Ca₃PN contributed mainly by Ca-d orbitals.²⁶ Near the Fermi energy level, I ions contribute 60.14%

to TDOS, Rb 20% and Pb only 19.79%, which is consistent with the contribution to the total λ and is a key factor in enhancing phonon-mediated superconductivity EPC. Regretfully, both Pb and I have large relative atomic masses, which drag down the average value of RbPbI₃ atomic vibration frequency, making $\langle\omega^2\rangle$ smaller. These factors lead to a strong electro-acoustic coupling interaction in RbPbI₃ and also suggest that the superconductivity of RbPbI₃ is mainly contributed by I. Analogously, Na_{0.2}WO₃ in the M_xWO₃ system also has a superconducting transition temperature of 3 K,^{26,59,60} which is slightly lower than that of RbPbI₃ with 8 K at 20 GPa. Our findings may further promote to explore high-temperature low-pressure superconductors and also need further experiment to verify the accuracy of our calculations.

4 Summary

The first-principles calculations conjunct with the particle swarm optimization algorithm are performed to explore the structural evolution, electronic properties, and superconductivity of RbPbI₃ at 0-100 GPa. Results indicate that RbPbI₃ undergoes a rich structural evolution by tuning the hydrostatic pressure. Two first-order reconstruction phase transitions from ppPv-*Pnma* to ppPv-*Pnma*(I) and from ppPv-*Pnma*(V) to *Pm* phases, as well as a second-order isomorphic phase transition from ppPv-*Pnma*(I) to ppPv-*Pnma*(V) were predicted, respectively. Notably, details of structural characteristics indicate that, whether ppPv-*Pnma*(V) or *Pm* phases, are two novel phases different from the previously reported ppPv-*Pnma*(I), ppPv-*Pnma*(II), ppPv-*Pnma*(III), ppPv-*Pnma*(IV) or *Pm*. Consequently, by tuning the pressure from 0 to 18 GPa, the insulator-to-semiconductor-to-metal transitions occur resulting in an obvious piezochromic effect. More importantly, a superconducting transition temperature of 8 K (7.3 K) at 20 GPa of the ppPv-*Pnma*(V) phase is predicted, implying RbPbI₃ is a potential low-pressure superconducting material. Undoubtedly, the p orbitals in I significantly contribute to the observed piezochromic effects and the emergence of superconductivity. These outstanding properties will stimulate experimental interest, potentially catalyzing additional investigations into novel superconductivity phenomena. Furthermore, this prompts further exploration of high- T_c low-pressure superconductivity of halide perovskites and their potential in scientific applications.

Conflicts of interest

There are no conflicts to declare.

Acknowledgements

This work is financially supported by the Central Government Funds of Guiding Local Scientific and Technological Development for Sichuan Province (No. 2021ZYD0026) and the National Natural Science Foundation of China (Nos. 11874043 and 12104416). H.T. thanks for the support of Zhengzhou Normal University Young Backbone Teacher Training Project (QNGG-221971).

Notes and references

- 1 W. Zhao, R. Su, Y. Huang, J. Wu, C. F. Fong, J. Feng and Q. Xiong, *Nat. Commun.*, 2020, **11**, 5665.
- 2 L. Protesescu, S. Yakunin, M. I. Bodnarchuk, F. Krieg, R. Ca-

- puto, C. H. Hendon, R. X. Yang, A. Walsh and M. V. Kovalenko, *Nano Lett.*, 2015, **15**, 3692–3696.
- 3 H. Zhu, M. T. Trinh, J. Wang, Y. Fu, P. P. Joshi, K. Miyata, S. Jin and X.-Y. Zhu, *Adv. Mater.*, 2017, **29**, 1603072.
- 4 Y. Hu, F. Bai, X. Liu, Q. Ji, X. Miao, T. Qiu and S. Zhang, *ACS Energy Lett.*, 2017, **2**, 2219–2227.
- 5 R. J. Sutton, M. R. Filip, A. A. Haghighirad, N. Sakai, B. Wenger, F. Giustino and H. J. Snaith, *ACS Energy Lett.*, 2018, **3**, 1787–1794.
- 6 M. Tai, C. F. J. Lau, H. Lin and Z. Wang, *Sol. RRL*, 2020, **4**, 2000495.
- 7 A. K. Jena, A. Kulkarni, Y. Sanehira, M. Ikegami and T. Miyasaka, *Chem. Mater.*, 2018, **30**, 6668–6674.
- 8 D. Liu, W. Zha, Y. Guo and R. Sa, *ACS Omega*, 2020, **5**, 893–896.
- 9 C. Abia, C. A. Lopez, J. Gainza, J. E. F. S. Rodrigues, M. M. Ferrer, G. Dalenogare, N. M. Nemes, O. J. Dura, J. L. Martinez, M. T. Fernandez-Diaz, C. Alvarez Galvan and J. A. Alonso, *Inorg. Chem.*, 2022, **61**, 5502 – 5511.
- 10 S.-H. Turren-Cruz, M. Saliba, M. T. Mayer, H. Juarez-Santesteban, X. Mathew, L. Nienhaus, W. Tress, M. P. Erodici, M.-J. Sher, M. G. Bawendi, M. Gratzel, A. Abate, A. Hagfeldt and J.-P. Correa-Baena, *Energy Environ. Sci.*, 2018, **11**, 78 – 86.
- 11 M.-H. Jung, S. H. Rhim and D. Moon, *Sol. Energy Mater Sol. Cells*, 2017, **172**, 44 – 54.
- 12 D. Amgar, T. Binyamin, V. Uvarov and L. Etgar, *Nanoscale*, 2018, **10**, 6060–6068.
- 13 S. Kumavat, D. Singh, Y. Sonvane and S. Gupta, *AIP Conf Proc*, 2019, **2115**, 030154.
- 14 P. Pansa-Ngat, K. Singh, B. Patel, C. Seriwattanachai, P. Kanjanaboos and O. Voznyy, *Chem. Mater.*, 2023, **35**, 271–279.
- 15 D. Andres-Penares, J. Navarro-Arenas, R. I. Sánchez-Alarcón, R. Abargues, J. P. Martínez-Pastor and J. F. Sánchez-Royo, *Appl. Surf. Sci.*, 2021, **536**, 147939.
- 16 S. Mitro, M. Saiduzzaman, A. Biswas, A. Sultana and K. M. Hossain, *Mater. Today Commun.*, 2022, **31**, 103532.
- 17 X. Wang, H. Tian, X. Li, H. Sang, C. Zhong, J.-M. Liu and Y. Yang, *Phys. Chem. Chem. Phys.*, 2021, **23**, 3479–3484.
- 18 M. Murakami, K. Hirose, K. Kawamura, N. Sata and Y. Ohishi, *Science*, 2004, **304**, 855–858.
- 19 C. Xu, B. Xu, Y. Yang, H. Dong, A. R. Oganov, S. Wang, W. Duan, B. Gu and L. Bellaiche, *Phys. Rev. B*, 2015, **91**, 020101.
- 20 A. C. Garcia-Castro, N. A. Spaldin, A. H. Romero and E. Bousquet, *Phys. Rev. B*, 2014, **89**, 104107.
- 21 H. Cheng, A.-J. Mao, X.-R. Cheng, H. Tian, X.-L. Dou, S.-M. Yang and X.-Y. Kuang, *J. Phys. Condens. Matter*, 2019, **31**, 505406.
- 22 H. Tian, X.-Y. Kuang, A.-J. Mao, Y. Yang, C. Xu, S. O. Sayedaghaee and L. Bellaiche, *Phys. Rev. B*, 2018, **97**, 020103.
- 23 A. P. Drozdov, M. I. Eremets, I. A. Troyan, V. Ksenofontov and S. I. Shylin, *NATURE*, 2015, **525**, 73+.
- 24 F. Peng, Y. Sun, C. J. Pickard, R. J. Needs, Q. Wu and Y. Ma, *Phys. Rev. Lett.*, 2017, **119**, 107001.
- 25 Z. Hui, X. Tang, D. Shao, H. Lei, J. Yang, W. Song, H. Luo, X. Zhu and Y. Sun, *Chem. Commun.*, 2014, **50**, 12734–12737.
- 26 H. Cheng, A.-J. Mao, S.-M. Yang, H. Tian, S.-Y. Jin, M. Yu and X.-Y. Kuang, *J. Mater. Chem. C*, 2020, **8**, 13072–13078.
- 27 A. Iyo, H. Fujihisa, Y. Gotoh, S. Ishida, H. Ninomiya, Y. Yoshida, H. Eisaki, H. T. Hirose, T. Terashima and K. Kawashima, *Inorganic Chemistry*, 2020, **59**, 12397–12403.
- 28 J. Song, Y. Qin, Y. Wang and C. Cao, *Phys. Chem. Chem. Phys.*, 2022, **24**, 1770–1778.
- 29 T. Kong, K. Gornicka, S. Golab, B. Wiendlocha, T. Klimczuk and R. J. Cava, *J. Phys. Soc. Japan*, 2018, **87**, 074711.
- 30 G. Kresse and J. Furthmüller, *Phys. Rev. B*, 1996, **54**, 11169–11186.
- 31 P. Hohenberg and W. Kohn, *Phys. Rev.*, 1964, **136**, B864–B871.
- 32 Y. Wang, J. Lv, L. Zhu and Y. Ma, *Comput Phys Commun*, 2012, **183**, 2063–2070.
- 33 Y. Wang, J. Lv, L. Zhu and Y. Ma, *Phys. Rev. B*, 2010, **82**, 094116.
- 34 J. P. Perdew, K. Burke and M. Ernzerhof, *Phys. Rev. Lett.*, 1996, **77**, 3865–3868.
- 35 H. J. Monkhorst and J. D. Pack, *Phys. Rev. B*, 1976, **13**, 5188–5192.
- 36 P. E. Blöchl, *Phys. Rev. B*, 1994, **50**, 17953–17979.
- 37 K. Momma and F. Izumi, *J Appl Crystallogr*, 2011, **44**, 1272 – 1276.
- 38 H. Stokes and D. Hatch, *J Appl Crystallogr*, 2005, **38**, 237–238.
- 39 S. Y. Savrasov, *Phys. Rev. B*, 1996, **54**, 16470–16486.
- 40 P. Giannozzi, S. Baroni, N. Bonini, M. Calandra, R. Car, C. Cavazzoni, D. Ceresoli, G. L. Chiarotti, M. Cococcioni, I. Dabo, A. Dal Corso, S. De Gironcoli, S. Fabris, G. Fratesi, R. Gebauer, U. Gerstmann, C. Gougoussis, A. Kokalj, M. Lazzeri, L. Martin-Samos, N. Marzari, F. Mauri, R. Mazzarello, S. Paolini, A. Pasquarello, L. Paulatto, C. Sbraccia, S. Scandolo, G. Sclauzero, A. P. Seitsonen, A. Smogunov, P. Umari and R. M. Wentzcovitch, *J. Phys. Condens. Matter*, 2009, **21**, 395502.
- 41 P. B. Allen and R. C. Dynes, *Phys. Rev. B*, 1975, **12**, 905–922.
- 42 S. Zhou, X. Kuang, F. Kuang, J. Qiu, M. Yu, J. Chen, J. Ma, Y. Li, F. Tang and A. Mao, *J. Phys. Chem. C*, 2023, **127**, 13346–13355.
- 43 Y. Li, X. Gong, P. Zhang and X. Shao, *Chem. Phys. Lett*, 2019, **716**, 76 – 82.
- 44 Y. Huang, Z. Hu, K. Li and X. Shao, *Comput. Mater. Sci.*, 2018, **143**, 403 – 410.
- 45 W. C. Kerr, A. M. Hawthorne, R. J. Gooding, A. R. Bishop and J. A. Krumhansl, *Phys. Rev. B*, 1992, **45**, 7036–7053.
- 46 N. Ni, S. Nandi, A. Kreyssig, A. I. Goldman, E. D. Mun, S. L. Bud'ko and P. C. Canfield, *Phys. Rev. B*, 2008, **78**, 014523.
- 47 J. Qiu, X. Kuang, M. Yu, Z. Xing, S. Zhou, J. Chen, J. Ma and A. Mao, *Phys. Chem. Chem. Phys.*, 2022, **24**, 22038 – 22045.
- 48 X.-R. Cheng, X.-Y. Kuang, H. Cheng, H. Tian, S.-M. Yang,

- M. Yu, X.-L. Dou and A.-J. Mao, *RSC Adv.*, 2020, **10**, 12432–12438.
- 49 F. Ke, J. Yan, S. Niu, J. Wen, K. Yin, H. Yang, N. R. Wolf, Y.-K. Tzeng, H. Karunadasa, I. Y. S. Lee, W. L. Mao and Y. Lin, *Nat. Commun.*, 2022, **13**, 7067.
- 50 D. Sando, Y. Yang, E. Bousquet, C. Carretero, V. Garcia, S. Fusil, D. Dolfi, A. Barthelemy, P. Ghosez, L. Bellaiche and M. Bibes, *NATURE COMMUNICATIONS*, 2016, **7**, year.
- 51 F. Peng, Y. Sun, C. J. Pickard, R. J. Needs, Q. Wu and Y. Ma, *Phys. Rev. Lett.*, 2017, **119**, 107001.
- 52 D. Duan, Y. Liu, F. Tian, D. Li, X. Huang, Z. Zhao, H. Yu, B. Liu, W. Tian and T. Cui, *Sci. Rep.*, 2014, **4**, 6968.
- 53 P. B. Allen and R. C. Dynes, *Phys. Rev. B*, 1975, **12**, 905–922.
- 54 W. L. McMillan, *Phys. Rev.*, 1968, **167**, 331–344.
- 55 J. Zheng, W. Sun, X. Dou, A.-J. Mao and C. Lu, *J. Phys. Chem. C*, 2021, **125**, 3150–3156.
- 56 X.-W. Yi, Z.-W. Liao, J.-Y. You, B. Gu and G. Su, *ISO 4*, 2023, **26**, 105813.
- 57 M. Gao, Z.-Y. Lu and T. Xiang, *Phys. Rev. B*, 2015, **91**, 045132.
- 58 A. Marronnier, H. Lee, B. Geffroy, J. Even, Y. Bonnassieux and G. Roma, *The Journal of Physical Chemistry Letters*, 2017, **8**, 2659–2665.
- 59 C.-S. Lian, C. Si, J. Wu and W. Duan, *Phys. Rev. B*, 2017, **96**, 235426.
- 60 K. Sano, Y. Nitta and Y. no, *J. Phys. Soc. Japan*, 2020, **89**, 113704.